Icarus 306 (2018) 139–149

Contents lists available at ScienceDirect

Icarus

journal homepage: www.elsevier.com/locate/icarus

The Apollo peak-ring impact basin: Insights into the structure and evolution of the South Pole–Aitken basin

Ross W.K. Potter[a,*], James W. Head[a], Dijun Guo[a,b,c], Jianzhong Liu[b,c], Long Xiao[d]

[a] Department of Earth, Environmental and Planetary Sciences, Brown University, Providence, RI 02912, USA
[b] Center for Lunar and Planetary Science, Institute of Geochemistry, Chinese Academy of Sciences, 99 Lincheng West Road, Guiyang 550051, China
[c] University of Chinese Academy of Sciences, Beijing 100049, China
[d] Planetary Science Institute, China University of Geosciences, Wuhan 430074, China

ARTICLE INFO

Article history:
Received 4 June 2017
Revised 27 January 2018
Accepted 2 February 2018
Available online 9 February 2018

Keywords:
Cratering
Impact processes
Moon, surface
Moon, interior

ABSTRACT

The 492 km-diameter Apollo impact basin post-dates, and is located at the inner edge of, the ~2240 km-diameter South Pole–Aitken (SPA) basin, providing an opportunity to assess the SPA substructure and lateral heterogeneity. Gravity Recovery and Interior Laboratory gravity data suggest an average crustal thickness on the floor of SPA of ~20 km and within the Apollo basin of ~5 km, yet remote sensing data reveal no conclusive evidence for the presence of exposed mantle material. We use the iSALE shock physics code to model the formation of the Apollo basin and find that the observational data are best fit by the impact of a 40 km diameter body traveling at 15 km/s into 20–40 km thick crustal material. These results strongly suggest that the Apollo impact occurred on ejecta deposits and collapsed crustal material of the SPA basin and could help place constraints on the location, size and geometry of the SPA transient cavity. The peak ring in the interior of Apollo basin is plausibly interpreted to be composed of inwardly collapsed lower crustal material that experienced peak shock pressures in excess of 35 GPa, consistent with remote sensing observations that suggest shocked plagioclase. Proposed robotic and/or human missions to SPA and Apollo would present an excellent opportunity to test the predictions of this work and address many scientific questions about SPA basin evolution and structure.

1. Introduction and background

The Apollo peak-ring impact basin (Fig. 1), with a diameter of 492 km (Baker et al., 2011; Baker and Head, 2015), is the largest definitive impact structure within the South Pole–Aitken (SPA) basin, the largest (2240 km diameter) lunar impact basin currently known. Originally classified as a multi-ring basin (Pike and Spudis, 1987), Apollo is now regarded as a peak-ring basin (Baker et al., 2011); its peak ring, rising 1–2 km above the basin floor, has a diameter of 247 km (Baker et al., 2011; Baker et al., 2017), a little over half the main rim diameter. On the basis of superposed impact crater counting (Stuart-Alexander, 1978), Apollo is one of the youngest pre-Nectarian basins (Wilhelms, 1987; Fassett et al., 2012), with an age of ~3.9–3.92 to 4.1–4.2 Ga.

Located in the north-east segment of SPA (Garrick-Bethell and Zuber, 2009) at 36.09°S, 208.52°E (Baker and Head, 2013), Apollo basin, as inferred by numerical modeling of the formation of SPA (Potter et al., 2012a), may straddle the SPA transient crater and modification zone (Fig. 1). Such a location may help explain the distinctive divide in mineralogy between Apollo basin's north and east (more anorthositic; Garrick-Berthell and Zuber, 2009) and south and west (more noritic; Pieters et al., 2001) sections.

Apollo basin sits largely within the SPA Heterogeneous Annulus (HET-A) zone (Fig. 1), defined by Moriarty and Pieters (2016) as localized areas exhibiting mafic signatures heterogeneously mixed with more feldspathic areas. The HET-A region contains discontinuous areas of Mg pyroxene-rich material, interpreted to represent ejected sub-crustal materials mixed with feldspathic crust during SPA ejecta emplacement and basin modification. The southern portion of Apollo sits within the SPA Orthopyroxene Annulus (OPX-A; Fig. 1.), defined by Moriarty and Pieters (2016) as areas where spectral analyses exhibit a homogenous composition consistent with (and dominated by) Mg-rich pyroxenes, interpreted to represent a remnant part of the SPA transient cavity that excavated through a ~40 km feldspathic crust. Whether the Mg pyroxene-rich material in the OPX-A and HET-A units represent upper mantle material (as predicted by cratering models; Potter et al., 2012a), or lower crust enriched in Mg-suite materials (Shearer et al., 2015) remains unanswered. Given Apollo's location, however, we would thus predict that the ejecta from the Apollo basin impact event

* Corresponding author.
E-mail addresses: ross_potter@brown.edu, rwkpotter@gmail.com (R.W.K. Potter).

https://doi.org/10.1016/j.icarus.2018.02.007
0019-1035/

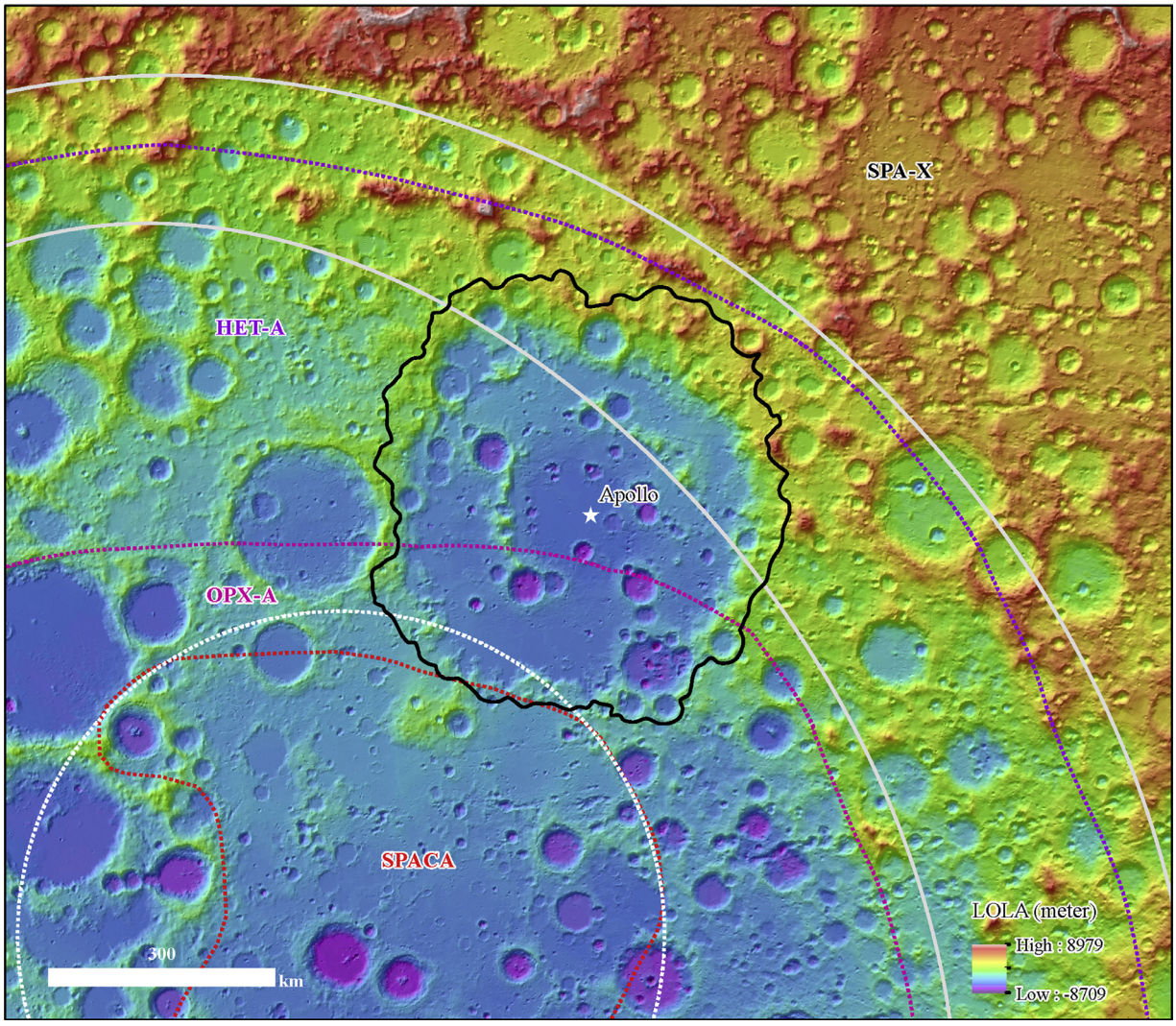

Fig. 1. Lunar Orbiter Laser Altimeter topographic map of the Apollo basin (outlined in black) region within the South Pole–Aitken (SPA) basin. Solid white lines illustrate the SPA topographic best-fit ellipses from Garrick-Bethell and Zuber (2009). The dashed white line illustrates the extent of the SPA transient crater from numerical modeling (Potter et al., 2012a). Dotted colored lines illustrate the extent of, from the SPA center, SPACA (SPA Compositional Anomaly; red), OPX-A (Orthopyroxene Annulus; light purple), HET-A (Heterogeneous Annulus; dark purple) and SPA-X (SPA Exterior) mineralogical zones (Moriarty and Pieters, 2016). (For interpretation of the references to color in this figure legend, the reader is referred to the web version of this article).

would have included Mg-rich pyroxenes interpreted to represent a remnant part of the SPA transient cavity.

Subsequent to the formation of the SPA and Apollo basins, mare deposits were emplaced and now partially cover the center of the basins (Yingst and Head, 1999; Pieters et al., 2001); older cryptomare deposits have been identified in the SPA basin interior (Pieters et al., 2001; Petro et al., 2011; Whitten and Head, 2015). Mare volcanism on the floor of the Apollo basin has been interpreted to date from ~2.4 to 3.5 Ga (Haruyama et al., 2009).

Clementine UVVIS data detected anorthosite ($>=90\%$ plagioclase) in the Apollo basin peak ring (Pieters et al., 2001), as did the Kaguya Multiband Imager (Ohtake et al., 2014). Ohtake et al., (2014) stated that the peak ring contained continuous exposures of pure anorthosite ($>98\%$ plagioclase). Moon Mineralogy Mapper (M^3) data, however, suggest that the peak ring is dominated by pyroxene ($<95\%$ plagioclase; Baker and Head, 2015), with the only pure anorthosite exposure located toward the basin rim (at an unnamed crater: 28.8491°S, 205.5807°E; Donaldson-Hanna et al., 2014). M^3 analysis of craters near the Apollo peak ring suggests the presence of Mg-rich material (Klima et al., 2011), consistent with the mafic-rich compositional interpretations of others (Petro et al., 2010; Baker and Head, 2015). These multispectral analyses, therefore, suggest that the Apollo-forming impact may have excavated primary crustal material (Petro et al., 2010; Klima et al., 2011), or a more magnesian region (such as an intrusion or cumulate pile; Klima et al., 2011). The crust beneath the center of Apollo is <5 km thick (Fig. 2, 3; Wieczorek et al., 2013), making it one of the thinnest crustal locations on the Moon. A strong positive Bouguer gravity signature (Neumann et al., 2015; Baker et al., 2017), suggesting denser material (i.e., mantle) close to the surface, further supports this. The thin crust beneath the basin center and possible presence of SPA Mg-rich pyroxene deposits (HET-A and OPX-A units) could explain the more mafic nature (Baker and Head, 2015) of the Apollo basin interior.

The age, geology and structure of Apollo make it a strong candidate for both robotic and human missions dedicated to studying early lunar processes and the structure of the SPA terrane (defined in Jolliff et al., 2000). Previously, Apollo was a region of interest for the NASA Constellation program (Gruener and Joosten, 2009). Recently, China has placed the Apollo basin as a possible candidate for its Chang'e-4 landing and roving mission, scheduled for launch in the first half of 2019 (Wang and Liu, 2016).

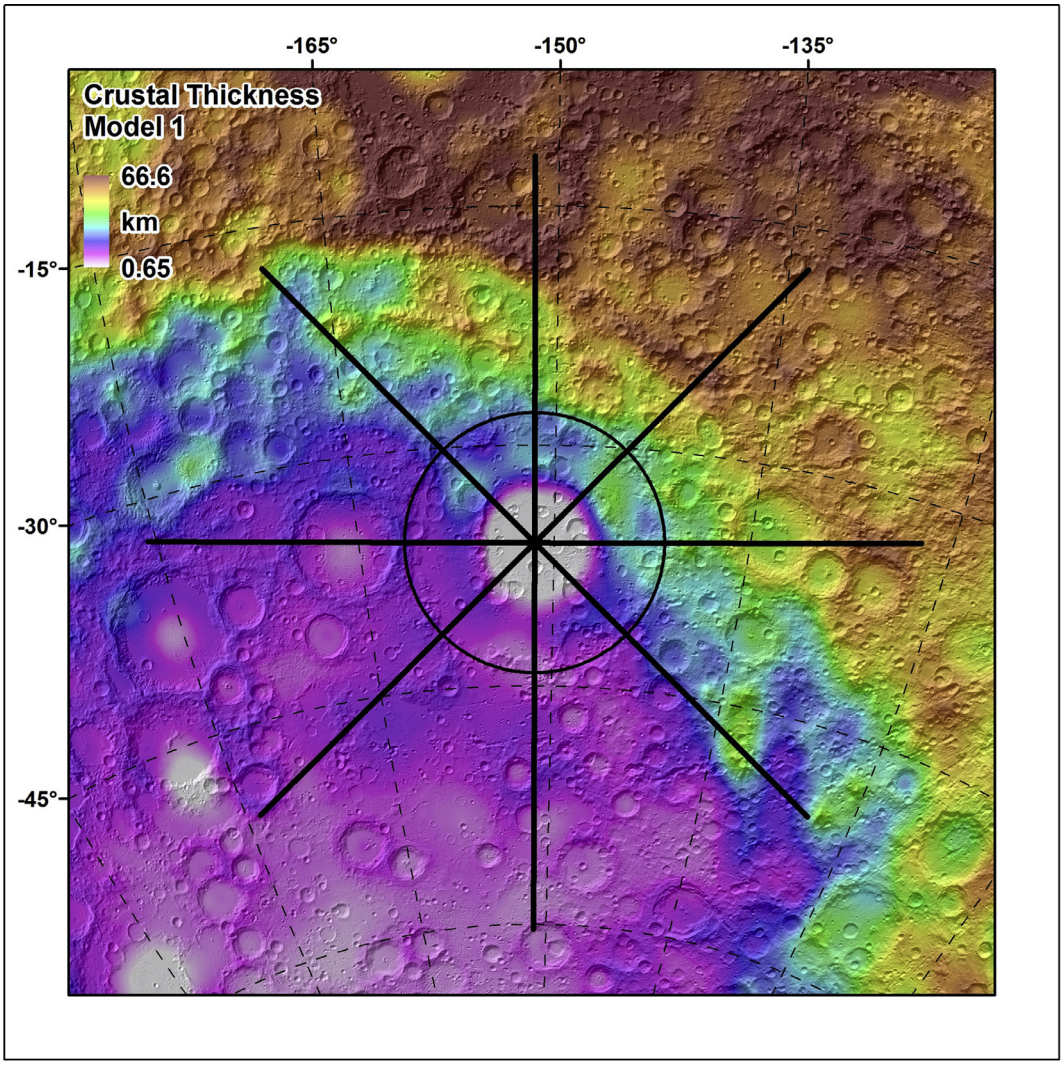

Fig. 2. Model 1 Gravity Recovery and Interior Laboratory-derived crustal thickness (Wieczorek et al., 2013) around Apollo basin, highlighting the crustal dichotomy between the north and east, and south and west sections. Cross-sectional profile markers are highlighted by the straight lines. A selection of these are shown in Fig. 3.

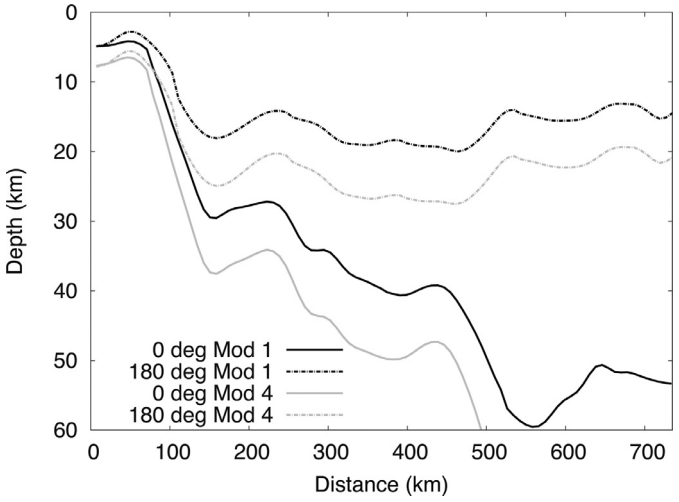

Fig. 3. Cross-sectional crustal thickness profiles through Apollo basin derived from Gravity Recovery and Interior Laboratory data for gravity models 1 and 4 (Wieczorek et al., 2013). 0° represents profiles from the basin center directly northward; 180° presents profiles from the basin center directly southward.

In this work, therefore, we numerically modeled the formation of the Apollo basin to understand (a) its unique geological structure, (b) how this structure relates to SPA's own structure and evolution, and (c) the importance of the Apollo basin for future lunar surface missions.

2. Methods

The two-dimensional iSALE shock physics code (Collins et al., 2004; Wünnemann et al., 2006) based upon the SALE hydrocode (Amsden et al., 1980), was used to simulate the formation of the Apollo basin. iSALE has been used extensively to model lunar basin formation (e.g., Potter et al., 2012a; 2012b; 2013; 2015; Miljković et al., 2013; 2016; Zhu et al., 2015; Johnson et al., 2016) and to investigate impacts on a wide range of scales. Relative to the Apollo basin, this includes smaller, simple craters (Collins, 2014); similar-sized basins (e.g., Schrödinger basin; Kring et al., 2016); and far larger basins (e.g., South Pole–Aitken basin; Potter et al., 2012a). The two-dimensionality of the code limits impact simulations to 90° (vertically downward). Although exactly vertical impacts are highly unlikely, they provide a reasonable proxy for oblique (~30–45°) impacts (e.g., Gault and Wedekind, 1978; Pierazzo and Melosh, 2000; Elbeshausen et al., 2009; Davison et al., 2011) and are interpreted to produce the correct azimuthally-averaged behavior.

Table 1
Selected model input parameters. Input parameters are listed in a more comprehensive manner in Supplementary Files S1 and S2.

Parameter	Value(s)
Impact velocity	10, 15 km/s
Impactor diameter	32, 40, 50, 60 km
Crust material	Gabbroic anorthosite Tillotson EOS (Ahrens and O'Keefe, 1977; Potter et al., 2012b)
Mantle material	Dunite ANEOS (Benz et al., 1989)
Crustal thickness	20, 40 km
Thermal gradient	10 K/km; mantle temperatures at solidus

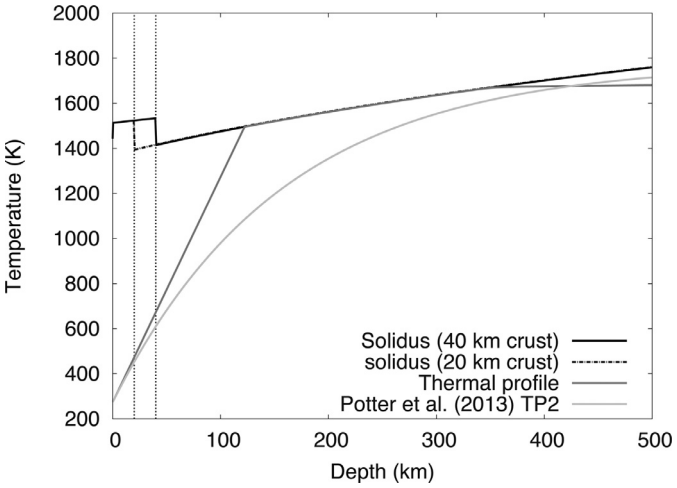

Fig. 4. Thermal profile used to present the lunar subsurface at the time of the Apollo basin-forming impact. Solidus profiles differ slightly depending on the crustal thickness (20 km or 40 km, illustrated by the two vertical dashed lines). A thermal profile from Potter et al. (2013) is shown for reference. Preliminary models were carried out using this thermal profile, but it was found to be too strong a target to produce Apollo basin-like features.

Impactor diameters of 32, 40, 50 and 60 km, and impact velocities of 10 and 15 km/s were used to find a best-fit (relative to spectroscopic and gravity data) impact scenario for Apollo basin. Due to the crustal dichotomy between the north-east and south-west sides of the basin (Wieczorek et al., 2013; Figs. 2 and 3), crustal thicknesses of 40 and 20 km, respectively, were used. Cell resolution was 1 km, providing 16–30 cells per projectile radius, consistent with a suite of other large crater-forming studies (e.g., Ivanov, 2005; Potter et al., 2015; Miljković et al., 2016). Following the initial analysis, the better fitting simulations were run at twice the original resolution (0.5 km per cell). See Table 1 for a list of the major model impact parameters.

The axisymmetric halfspace target was divided into a crustal and mantle layer. A Tillotson equation of state for gabbroic anorthosite (Ahrens and O' Keefe, 1977; Potter et al., 2012b) and a semi-analytical equation of state (ANEOS) for dunite (Benz et al., 1989) were used to represent the crust and mantle, respectively; the dunite ANEOS was also used to represent the impactor. The strength and thermal properties of these materials were taken from laboratory experiment data for gabbro (Azmon, 1967; Stesky et al., 1974; Shimada et al., 1983) and dunite (Shimada et al., 1983; Ismail and Murrell, 1990); curves for mantle melt temperature as a function of pressure for dunite were taken from Davison et al. (2010). The strength and damage models used here are described in Collins et al. (2004) and Ivanov et al. (2010), respectively; further information can be found in supplementary files S1 and S2.

Due to the age and location of Apollo, a thermal profile with a gradient of 10 K/km and upper mantle temperatures at the solidus (Potter et al., 2012a; Potter et al., 2013) was used (Fig. 4). This thermal profile is comparable to those used in other lunar basin formation studies (e.g., Miljković et al., 2013, 2016; Zhu et al., 2015) and was chosen as it represents a cooler thermal profile than that for the underlying, older SPA event (Potter et al., 2012a). As a first-order approximation to account for the rheology of partially molten material, and in line with previous lunar basin modeling studies (e.g., Potter et al., 2015), a partial melt viscosity of 10^{10} Pa s (Potter, 2012) was used. Additionally, acoustic fluidization (Melosh, 1979; Melosh and Ivanov 1999), a mechanism used to invoke deep-seated gravitational collapse of transient craters in large-scale impacts, was included via the block model (Melosh and Ivanov, 1999) and implemented following the approach of Potter et al. (2015). Gravitational acceleration was a constant 1.63 m/s^2.

3. Results

3.1. Structure

The structure of two Apollo-sized basins, that best fit spectroscopic and gravity data, after the dynamic phase of basin formation is complete (~80 min after the initial impact) is illustrated in Fig. 5. The impacts consisted of a 40 km diameter body traveling at 15 km/s and striking a (a) 20 km crust and (b) 40 km crust (representing the crustal dichotomy at Apollo). The figure highlights the distribution of tracer particles within each material unit (impactor material is shown in red; crust in blue; and mantle in green). For the 20 km crust scenario (Fig. 5a), a thin (1–2 km) layer of crustal material (with some impactor material mixed in) is discontinuously present on the basin floor from the basin center, through the peak ring zone, out to the basin rim zone (where crustal material dominates). A similarly thick, but more continuous, crustal layer is also present on the basin floor in the 40 km crust scenario (Fig. 5b). Supplementary files S3 and S4 are videos that demonstrate the basin-forming process for the best-fit impacts into the 20 and 40 km crust, respectively.

Excavation depths were ~31 km for both impacts, hence the greater presence of mantle material at the surface in the 20 km crust scenario. Excavation depth was calculated, following Potter et al. (2015), as the deepest pre-impact material that was above the pre-impact target surface on formation of the transient crater (the transient crater is defined as the impact-induced bowl-shaped cavity at maximum volume). These modeled excavation depths are similar to the estimates of Morrison (1998) - 28 km, Petro and Jolliff (2013) - 35 km, and Baker and Head (2015) - 38 km, all derived from scaling laws. Excavation depth-to-diameter ratios for all modeled scenarios (0.12 ± 0.01) are consistent with previous lunar crater and basin modeling (e.g., Potter et al., 2015). Transient crater diameters were ~250 km for both impacts. This is smaller than the scaling estimate of 315 km calculated by Miljkovic et al. (2016) (see Tables 1 and 2 in that work), however that study assumed a colder thermal profile and different scaling parameters. The numerical models, therefore, predict that the Apollo basin-forming impact would have excavated mantle material if crustal thickness was $<$ ~30 km, agreeing with previous studies (Petro and Jolliff, 2013; Baker and Head, 2015). Table 2

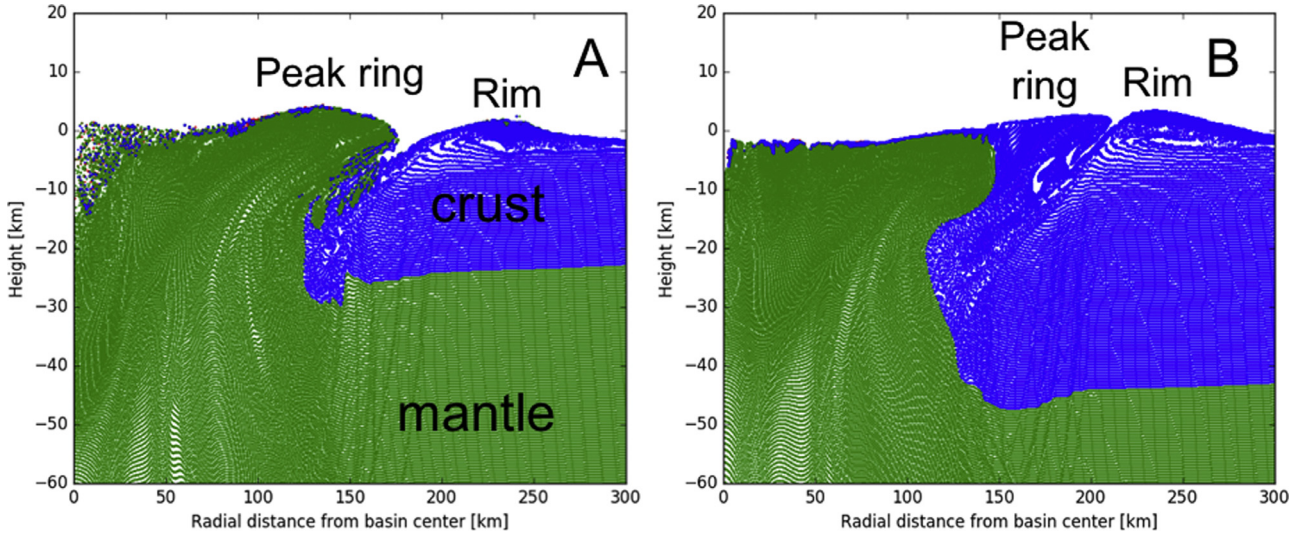

Fig. 5. Distribution of material tracers (impactor: red; crust: blue; mantle: green) for the best-fit Apollo basin models. These models considered the impact of a 40 km diameter body at 15 km/s into a (a) 20 km crust and (b) 40 km crust. Note the vertical exaggeration. White space indicates the absence of tracer particles. An overlay of this figure with the gravity-derived crustal thickness profiles (Fig. 3) can be found in the supplemental material (Fig. S6). (For interpretation of the references to color in this figure legend, the reader is referred to the web version of this article).

Table 2
Model results. Rows highlighted in bold represent the best-fit impacts for each of the crustal thicknesses. A more comprehensive data table can be found in supplementary file S5.

Crustal thickness (km)	Impactor diameter (km)	Impact velocity (km/s)	Impact energy (J)	Transient crater diameter, Dtc (km)	Excavation depth, Zex (km)	Zex/Dtc
40	40	10	5.53E + 24	219	28.5	0.130
40	50	10	1.08E + 25	255	32.5	0.127
40	60	10	1.87E + 25	291	36.5	0.125
40	60	10	1.87E + 25	296	36.75	0.124
40	32	15	6.37E + 24	217	27.5	0.127
40	40	15	1.24E + 25	251	31.5	0.125
40	**40**	**15**	**1.24E + 25**	**254**	**32.25**	**0.127**
20	32	10	2.83E + 24	185	18.5	0.100
20	40	10	5.53E + 24	203	23.5	0.116
20	50	10	1.08E + 25	239	30.5	0.128
20	60	10	1.87E + 25	285	36.75	0.129
20	32	15	6.37E + 24	201	23.5	0.117
20	40	15	1.24E + 25	237	30.5	0.129
20	**40**	**15**	**1.24E + 25**	**243**	**31.25**	**0.129**
20	50	15	2.43E + 25	279	37.5	0.134

lists a selection of attributes for the numerical models. Additional attributes are listed in supplementary file S5, with a direct comparison of the best-fit models and gravity-derived crustal thickness in supplemental file S6.

3.2. Peak shock pressure

The distribution of peak shock pressures in the upper few kilometers of the basin structure (−6 to + 6 km; a zone that could be possibly sampled in future missions) is illustrated in Fig. 6 for the same impact scenarios presented in Fig. 5. In the 20 km crust scenario (Fig. 6a, b), the peak ring zone (100–150 km radial distance) is dominated by mantle material (Fig. 6a) shocked in excess of 45 GPa (Fig. 6b). Of the material shocked below 45 GPa in the peak ring zone, ~65% of material is shocked below 15 GPa (Fig. 7a). Bands of lower peak shock pressures are present downwards of ~1 km elevation (Fig. 6b). Around the basin rim (~210–250 km radial distance), which is dominated by crustal material, 95% of the material is shocked below 15 GPa (relative to a 45 GPa shock pressure; Fig. 7b). Beyond the basin rim, some isolated crustal material is shocked > 20 GPa (Fig. 6b).

For the 40 km scenario (Fig. 6c, d), the surface peak shock pressures (of crust, mantle and impactor material; Fig. 6d) exceed 45 GPa from the basin center consistently out to a distance of 150 km. Around the peak ring zone (~150–200 km radial distance), crust is the dominant unit. Here, peak shock pressures vary by approximately one order of magnitude, with juxtaposition of notably different shock levels at depth (e.g., 20–25 GPa and > 45 GPa at a radial distance of 150 km). Of the material shocked below 45 GPa in the peak ring zone, around 85% is shocked below 15 GPa (Fig. 7c). Around the basin rim zone (210–240 km radial distance) peak shock pressures decrease with ~95% of material (relative to a 45 GPa shock pressure) shocked below 15 GPa (Fig. 7d).

3.3. Original depth of peak ring and rim material

Figs. 8 and 9 illustrate the (a, c) original and (b, d) final location for peak ring and basin rim material down to a depth of 6 km for the 20 km and 40 km crustal scenarios, respectively. For the 20 km crust (Fig. 8), peak ring material originates (Fig. 8a) mainly in the mantle, down to a ~70 km depth and up to 100 km from the basin center. In the 40 km scenario (Fig. 9a) the main origin of peak-ring material is the lower half of the crust (30–40 km depth), with only

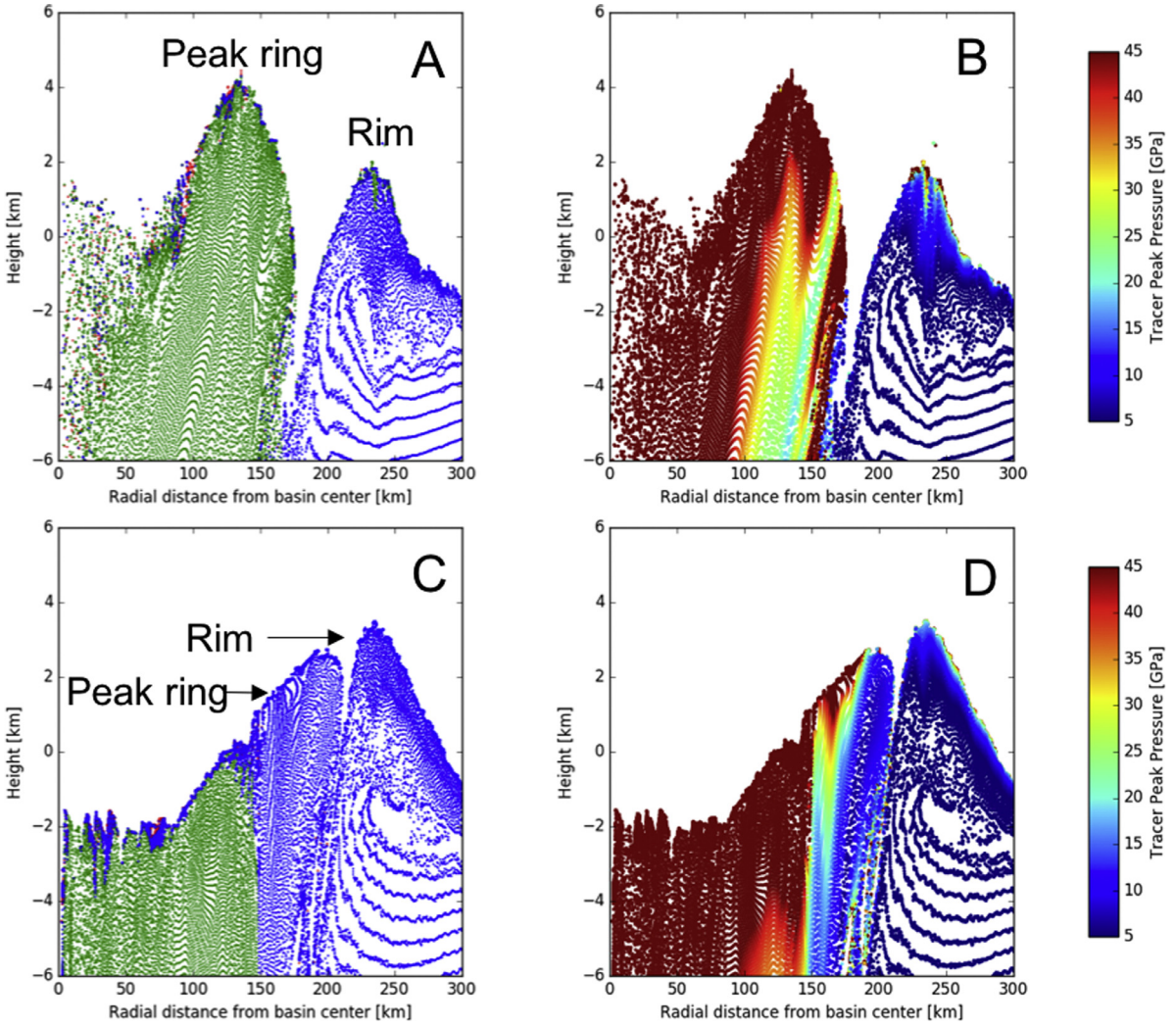

Fig. 6. Distribution of material tracers (impactor: red; crust: blue; mantle: green) – left panels – and peak shock pressure tracers – right panels – for the impact of a 40 km diameter body at 15 km/s into a (a, b) 20 km crust and (c, d) 40 km crust. Note the vertical exaggeration. White space indicates the absence of tracer particles. (For interpretation of the references to color in this figure legend, the reader is referred to the web version of this article).

a small fraction from the upper mantle. Consequently, the greater origin depth of the peak ring materials in the 20 km case explain the higher peak shock pressures, relative to the 40 km crustal case (Fig. 6).

Basin rim materials are sourced (Figs. 8c, 9c) from similar depths (~30 km) in both crustal scenarios and, therefore, have similar peak shock pressures (Fig 6). These depths are comparable to the excavation depth (31 km) and are noticeably shallower than the peak ring material origin. As with the peak ring material, the majority of rim material was displaced to the rim and was not originally *in-situ* (i.e., not present at the rim pre-impact). Over 90% of material is emplaced at the rim within the first 10 min of impact through deposition from the ejecta curtain and overturned rim (see supplementary videos S3 and S4). The remaining material is emplaced via collapse of the central uplift after ~30 min. Origin depths for both the peak ring and rim material are far shallower than that of the transient crater (maximum depth of ~132 km).

4. Discussion

4.1. Spectral and compositional interpretation

M^3 data (Baker and Head, 2015) suggest that the Apollo basin peak ring is dominated by Class C spectra (spectrally dominated by pyroxene absorptions) as it contains < 95% plagioclase and has no clear 1.25 µm plagioclase absorption signature (Cheek et al., 2013). The 40 km crust scenario presented here demonstrates that peak ring material is dominated by anorthosite (crust) that, at the surface, experienced peak shock pressures in excess of 35 GPa (Fig. 6c, d). This is high enough for plagioclase to lose its 1.25 µm absorption band and, therefore, match the observations of Baker and Head (2015). Additionally, the 20 km crust scenario, which excavates relatively more mantle material toward the surface, suggests the peak ring would be dominated by this mafic-rich mantle material. M^3 analysis of craters near the Apollo peak ring suggests the presence of Mg-rich material (Klima et al., 2011), further implying a more mafic, rather than plagioclase, composition.

The mafic-dominated composition of Apollo could be due to the size of impact (i.e., sampling depth) and its location within SPA, which consists of two Mg-rich pyroxene units (OPX-A and HET-A; Moriarty and Pieters, 2016). Using coordinates of 53.2°S, 191.1°E for the center of SPA (based on best-fit topographic ellipses; Garrick-Bethell and Zuber, 2009), Apollo is situated ~340 to ~840 km from SPAs center. Numerical modeling of the formation of SPA (Potter et al., 2012) suggested a transient crater with a radius of 420 km. Apollo basin may, therefore, straddle the SPA transient crater and modification zone (Fig. 1) - though others, e.g., Ohtake et al. (2014), suggest that the SPA melt pool, an analogy

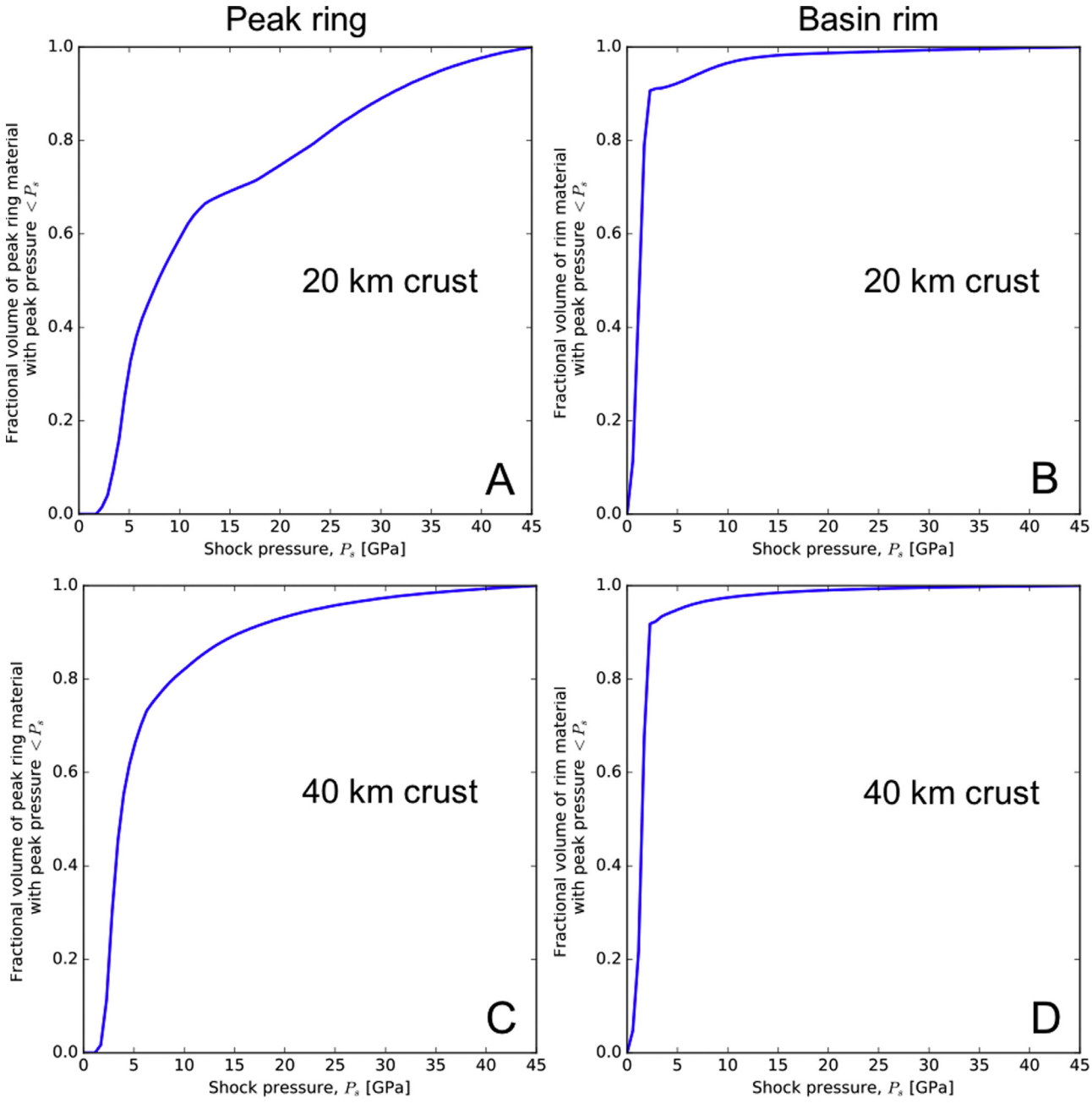

Fig. 7. Fractional volume of (a, c) peak ring and (b, d) basin rim material shocked below P_s, relative to the total volume shocked below 45 GPa for a 40 km diameter body impacting at 15 km/s into a (a, b) 20 km crust and (c, d) 40 km crust. The number of tracers sampled in each peak ring and rim zone is ~2000.

for the transient crater, had a smaller radius of 315–343 km. Such positioning means the Apollo impact may have formed in a target dominated by SPA excavated (Moriarty and Pieters, 2016) upper mantle material, possibly differentiated, with thinner crust toward SPAs center (the south-west side of Apollo). Additionally, scaling laws suggest that SPA ejecta thickness around the Apollo impact site could have been up to ~20 km (Equation 3 of McGetchin et al., 1973; exponent −2.8 from Fassett et al., 2011) at the sub-impact point of the Apollo basin. These results strongly suggest that the Apollo impact occurred on the ejecta deposits and collapsed crustal material of the SPA basin.

The numerical models demonstrate that a more mafic (i.e., lower crust and mantle) surface composition is more likely in the thinner crust scenario, i.e. closer to the SPA center. The size of the impact is great enough to excavate material from ~30 km, so in the case of the 20 km crust, this would include mantle material, hence the more mafic compositions on the south-west side of Apollo, closer to the center of SPA. The peak ring in the interior of Apollo basin is therefore likely composed of inwardly collapsed lower crustal material that experienced peak shock pressures in excess of 35 GPa, consistent with remote sensing observations. Additionally, the south-west portion of Apollo is situated within the SPA main Fe anomaly zone (~10 wt%) (Jolliff et al., 2000), which would further enhance mafic signatures around Apollo. The numerical models reported here suggest significant thinning of the crust beneath Apollo to ~1–2 km. Gravity Recovery and Interior Laboratory data (Wieczorek et al., 2013; Baker et al., 2017) suggest it could be slightly thicker (~5 km). Nevertheless,

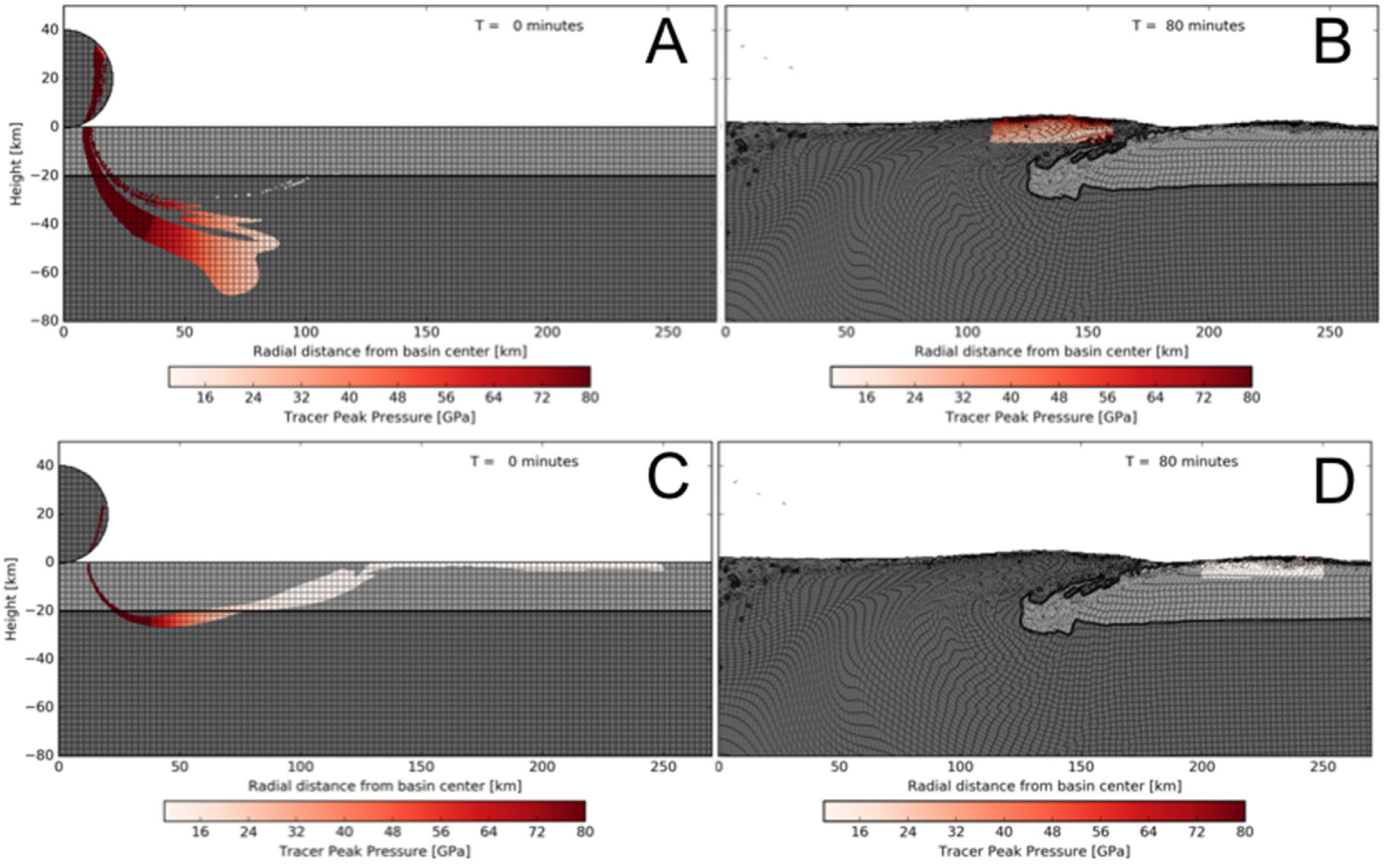

Fig. 8. Origin (left panels) and final (right panels) location of (a, b) peak-ring material and (c, d) basin rim material for a 40 km diameter body impacting at 15 km/s into a 20 km crust.

this demonstrates that the Apollo basin would have some of the thinnest crustal material on the Moon.

4.2. Thermal structure

The thermal profile used in this work has mantle temperatures at the solidus between depths of ~120 and ~360 km (Fig. 4). This thermal profile was chosen to represent a cool SPA sub-surface structure. With an estimated age of ~4.3 Ga (Morbidelli et al., 2012), SPA is the oldest confirmed lunar basin-forming impact. The impact would have created a large volume of melt (~10^7 km^3; Potter et al., 2012) that would have likely undergone differentiation (Hurwitz and Kring, 2014; Vaughan and Head, 2014). Given a 4.3 Ga age for SPA, Apollo (based on its inferred age Wilhems, 1987; Fassett et al., 2012) is likely to have formed ~200–300 Myr after SPA. Investigation of melt differentiation dynamics (Vaughan and Head, 2014; Cassanelli and Head, 2016), suggests that cooling of the SPA melt zone is unlikely to have lasted beyond a few million years, making it unlikely that the SPA melt sheet was molten when Apollo formed.

Impacts using an even cooler thermal profile (TP2 from Potter et al., 2013; Fig. 4), with mantle temperatures below the solidus were also carried out, but the target was found to be too strong to produce the features associated with Apollo. These basins were either too deep topographically or had crustal excesses (rather than deficits) at the basin center. The preferred thermal profile fits well with the thermal estimates for the younger Orientale (Potter et al., 2013; Zuber et al., 2016; Johnson et al., 2016) and Schrödinger basins (Kring et al., 2016) suggesting the same or a cooler, stronger target, when compared to Apollo, for these younger basins.

4.3. Schrödinger comparison

Apollo is not the only significant, well preserved, impact structure within SPA that may provide insight into SPA structure and evolution. Schrödinger basin, located in the opposite SPA sector relative to Apollo, is ~200–300 Myr younger (Wilhelms, 1987; Shoemaker et al., 1994) and approximately two-thirds (320 km) the diameter of Apollo. It is also commonly discussed as a potential site for future exploration (Bunte et al., 2011; O'Sullivan et al., 2011; Burns et al., 2013; Potts et al., 2015). Despite the smaller size of Schrödinger and its greater distance from the center of SPA (900 km), Kaguya remote sensing observations identified olivine exposures in its peak ring (Yamamoto et al., 2012); olivine exposures were not identified within Apollo (Yamamoto et al., 2010; Yamamoto et al., 2012). M^3 analysis of the Schrödinger olivines, in conjunction with Lunar Reconnaissance Orbiter camera and Lunar Orbiter Laser Altimeter data analysis, however, suggests they are troctolite (olivine and plagioclase), rather than true dunites (> 90% olivine), and, therefore, sourced from the crust rather than the mantle (Kring et al., 2016). The Schrödinger basin, as with Apollo, formed in the unit described by Moriarty and Pieters (2016) to be HET-A (localized areas exhibiting mafic signatures and heterogeneously mixed with more feldspathic areas outside the OPX-A zone, but inside the topographic basin rim of SPA). Unlike Schrödinger, Apollo is also partly located within the OPX-A region and, therefore, may have sampled (possibly differentiated) SPA transient crater material.

Schrödinger and Apollo have similar inferred pre-impact crustal thicknesses (25–40 km), but Schrödinger has a shallower excavation depth (19–23 km) and peak ring material from no more than 26 km deep (Kring et al., 2016). Schrödinger is, therefore,

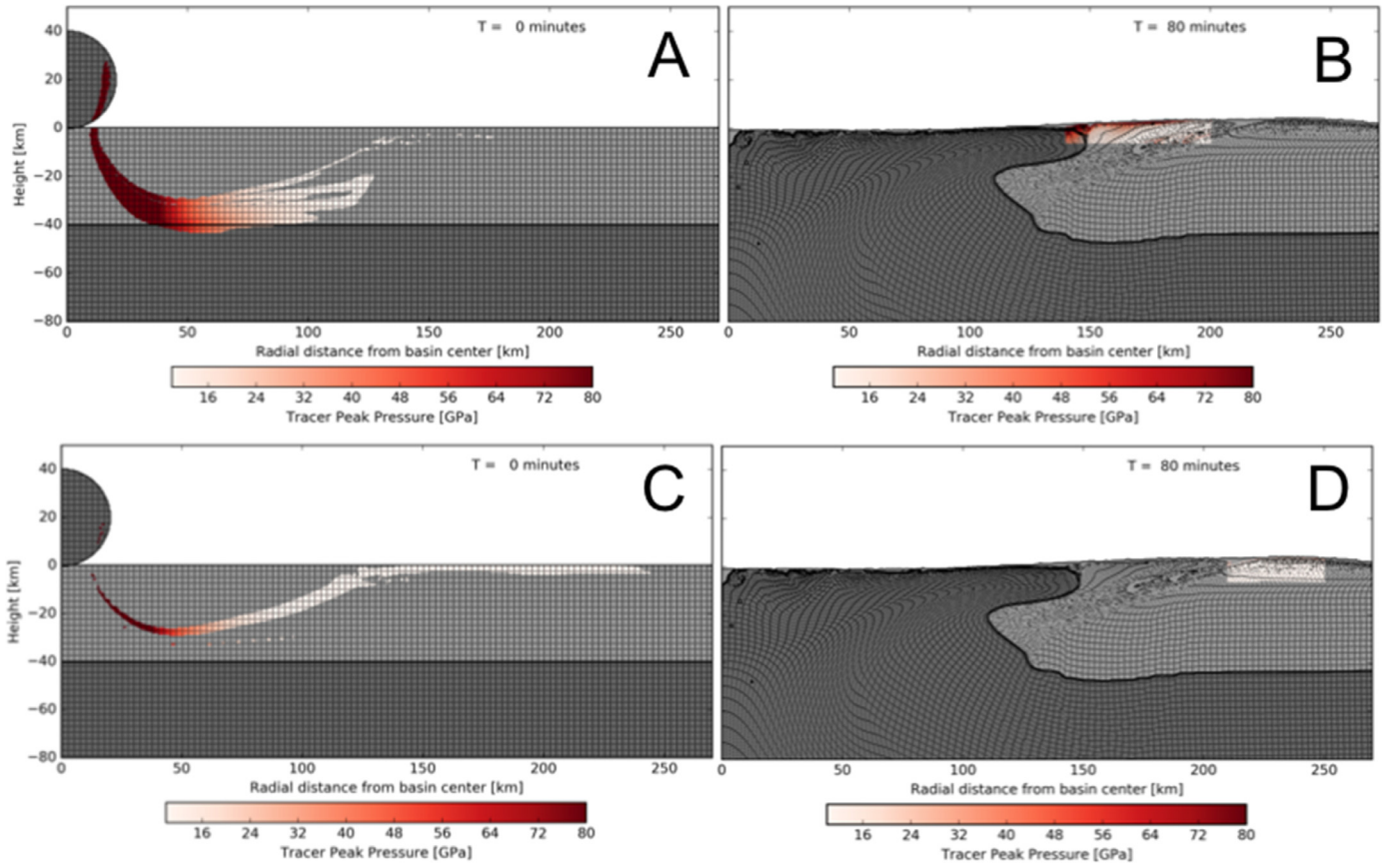

Fig. 9. Origin (left panels) and final (right panels) location of (a, b) peak-ring material and (c, d) basin rim material for a 40 km diameter body impacting at 15 km/s into a 40 km crust.

sampling on average a shallower part of the lunar subsurface than Apollo. The identification of (troctolitic) olivine at Schrödinger, but not at Apollo, suggests that the subsurface structure of SPA is a heterogeneous composition of melted layers (Morrison, 1998; Yamamoto et al., 2012). Such heterogeneity may exist across Apollo itself based on the distribution of anorthositic and mafic material. The Apollo peak ring, based on the numerical models, samples materials from 30 + km depth, however peak ring materials are not interpreted as mantle (e.g., Klima et al., 2011). This implies that the mafic content (on the thinner-crust, south-western side of the basin), may represent primary crust (Petro et al., 2010; Klima et al., 2011) or a more magnesian-rich lower crustal region (Klima et al., 2011), possibly associated with the SPA transient crater and melt pool cooling and differentiation.

4.4. Exploration

Given the structure of Apollo basin inferred from this and previous studies, exploration of Apollo would greatly enhance understanding of the SPA terrane and early lunar processes. Sampling opportunities for both mafic and anorthositic materials, in close proximity, would be possible in the basin peak ring. Some of the more mafic units in the peak ring could have originated beneath the crust and sampled mantle, a cumulate pile, or primary crust. Important goals for future missions to the SPA terrane would be: 1) analysis of sub-SPA mantle material; 2) assessment of the mineralogy of peak rings to constrain basin numerical models; 3) analysis of the mineralogy and age of farside mare basalts derived from unsampled deep mantle and erupted through thin-to-nonexistent crust; 4) mineralogy and petrology of unique farside materials; 5) geophysical structure of a peak ring basin; and 6) further understanding of the nature of the SPA basin. If chosen as the landing destination for the Chinese Chang' e-4 mission (Wang and Liu, 2016), Apollo basin would represent a superb opportunity to start addressing these goals and be the first mission to sample material not only within SPA but on the lunar farside. Due to the size of SPA, exploration of Apollo would be complemented by any future exploration of Schrödinger (O'Sullivan et al., 2011; Burns et al., 2013; Potts et al., 2015) as well as the proposed MoonRise sample return mission to the SPA interior (Jolliff et al., 2017). Together, samples from Apollo and Schrödinger basin would represent material from opposite sectors of SPA and would help to constrain the (probable) mineralogical heterogeneity across the basin.

5. Conclusions

Apollo basin is the largest definitive impact structure within the largest confirmed impact basin on the Moon, South Pole–Aitken (SPA). Numerical modeling of the formation of the Apollo peak-ring basin demonstrates that the final basin structure would have been greatly dependent on the impact site crustal thickness and material composition. This, in turn, would have been dependent on the formation of the SPA basin; spectral and numerical modeling studies imply Apollo may straddle the transient crater and modification zone of SPA. The numerical models, constrained by gravity-derived crustal profiles, demonstrate the Apollo basin-forming impact would have excavated material down to a depth of ~30 km. Thinner crust (~20 km) to the south and west of Apollo should lead to the excavation of sub-crustal material, possibly exposing it in the Apollo peak ring. The near-surface material in the modeled peak ring, using a 20 km crust, is mainly represented by greatly shocked (> 45 GPa) mantle. No definitive mantle ma-

terial has been identified at Apollo using remote sensing data, suggesting that material at such depths may represent a mafic-rich primary crust or cumulate pile. A dearth of pure anorthosite in M^3 data at the Apollo peak ring is likely explained by the magnitude of the impact, shocking crustal material above 15–25 GPa, erasing the anorthosite 1.25 µm absorption band. This suggests, therefore, that the Apollo impact occurred on the ejecta deposits and collapsed crustal material of the SPA basin and could help place constraints on the location, size and geometry of the SPA transient cavity. Comparisons with observations at Schrödinger basin, on the opposite side of SPA, suggest that the SPA subsurface structure is likely to be heterogeneous, and may exhibit smaller-scale heterogeneity across individual features, such as Apollo. Future missions to Apollo, which may include the Chinese Chang'e-4 mission, would provide crucial data for further understanding Apollo and the structure and evolution of the South Pole–Aitken basin.

Acknowledgments

We gratefully acknowledge financial support from the NASA Solar System Exploration Research Virtual Institute (SSERVI) grant for Evolution and Environment of Exploration Destinations under cooperative agreement number NNA14AB01A at Brown University. We thank Gareth Collins, Boris Ivanov, Jay Melosh, Kai Wünnemann and Dirk Elbeshausen for their work developing iSALE; further information about the code can be found at http://www.isale-code.de. Some plots in this work were created with the pySALEPlot tool written by Thomas M. Davison. We thank David Hollibaugh Baker for fruitful discussions and providing topographic and crustal thickness data across Apollo basin, and Daniel Moriarty for providing SPA mineralogy data. We thank the editor and an anonymous reviewer for their comments.

Supplementary materials

Supplementary material associated with this article can be found, in the online version, at doi:10.1016/j.icarus.2018.02.007.

References

Ahrens, T.J., O'Keefe, J.D., 1977. Equations of state and impact-induced shock-wave attenuation on the moon. In: Roddy, D.J., Peppin, R.O., Merrill, R.B. (Eds.), Impact and Explosion Cratering. Pergamon Press, New York, pp. 639–656.

Amsden, A.A., Ruppel, H.M., Hirt, C.W., 1980. SALE: A Simplified ALE Computer Program for Fluid Flow at all Speeds. Los Alamos National Laboratories Report LA-8095. LANL, Los Alamos, New Mexico. 101.

Azmon, E., 1967. The melting of gabbro up to 45 kg bars. NSL, 67–224.

Baker, D.M.H., Head, J.W., 2013. New morphometric measurements of craters and basins on Mercury and the Moon from MESSENGER and LRO altimetry and image data: an observational framework for evaluating models of peak-ring basin formation. Planet. Space Sci. 86, 91–116. doi:10.1016/j.pss.2013.07.003.

Baker, D.M.H., Head, J.W., 2015. Constraints on the depths of origin of peak rings on the Moon from Moon mineralogy mapper data. Icarus 258, 164–180. doi:10.1016/j.icarus.2015.06.013.

Baker, D.M.H., Head, J.W., Fassett, C.I., Kadish, S.J., Smith, D.E., Zuber, M.T., Neumann, G.A., 2011. The transition from complex crater to peak-ring basin on the Moon: new observations from the lunar orbiter laser altimeter (LOLA) instrument. Icarus 214, 377–393. doi:10.1016/j.icarus.2011.05.030.

Baker, D.M.H., Head, J.W., Phillips, R.J., Neumann, G.A., Bierson, C.J., Smith, D.E., Zuber, M.T., 2017. GRAIL gravity observations of the transition from complex cater to peak-ring basin on the Moon: implications for crustal structure and impact basin formation. Icarus 292, 54–73. doi:10.1016/j.icarus.2017.03.024.

Benz, W., Cameron, A.G.W., Melosh, H.J., 1989. The origin of the Moon and the single-impact hypothesis III. Icarus 81, 113–131. doi:10.1016/0019-1035(89)90129-2.

Bunte, M.K., Porter, S., Robinson, M.S., 2011. A sortie mission to Schrödinger basin as reconnaissance for future exploration. In: Garry, W.B., Bleacher, J.E. (Eds.). In: Analogs for Planetary Exploration, 483. Geological Society of America, pp. 533–546. doi:10.1130/2011.2483(32), Special Paper.

Burns, J.O., Kring, D.A., Hopkins, J.B., Norris, S., Lazio, T.J.W., Kasper, J., 2013. A lunar L2-Farside exploration and science mission concept with the Orion multipurpose crew vehicle and a teleoperated lander/rover. Adv. Space Res. 52, 306–320. doi:10.1016/j.asr.2012.11.016.

Cassanelli, J.P., Head, J.W., 2016. Did the orientale impact melt sheet undergo large-scale igneous differentiation by crystal settling. Geophys. Res. Lett. 43, 11156–11165. doi:10.1002/2016GL070425.

Cheek, L.C., Donaldson-Hanna, K.L., Pieters, C.M., Head, J.W., Whitten, J.L., 2013. The distribution and purity of anorthosite across the Orientale basin: new perspectives from Moon mineralogy mapper data. J. Geophys. Res. Planets 118, 1805–1820. doi:10.1002/jgre.20126.

Collins, G.S., 2014. Numerical simulations of impact crater formation with dilatancy. J. Geophys. Res. 119, 2600–2619. doi:10.1002/2014JE004708.

Collins, G.S., Melosh, H.J., Ivanov, B.A., 2004. Modeling damage and deformation in impact simulations. Meteorit. Planet. Sci. 39, 217–231. doi:10.1111/j.1945-5100.2004.tb00337.x.

Davison, T.M., Collins, G.S., Ciesla, F.J., 2010. Numerical modeling of heating in porous planetesimal collisions. Icarus 208, 468–481. doi:10.1016/j.icarus.2010.01.034.

Davison, T.M., Collins, G.S., Elbeshausen, D., Wünnemann, K., Kearsley, A., 2011. Numerical modeling of oblique hypervelocity impacts on strong ductile targets. Meteorit. Planet. Sci. 46, 1510–1524. doi:10.1111/j.1945-5100.2011.01246.x.

Donaldson-Hanna, K.L., Cheek, L.C., Pieters, C.M., Mustard, J.F., Greenhagen, B.T., Thomas, I.R., Bowles, N.E., 2014. Global assessment of pure crystalline plagioclase across the Moon and implications for the evolution of the primary crust. J. Geophys. Res. Planets 119, 1516–1545. doi:10.1002/2013JE004476.

Elbeshausen, D., Wünnemann, K., Collins, G.S., 2009. Scaling of oblique impacts in frictional targets: implications for crater size and formation mechanisms. Icarus 204, 716–731. doi:10.1016/j.icarus.2009.07.018.

Fassett, C.I., Head, J.W., Smith, D.E., Zuber, M.T., Neumann, G.A., 2011. Thickness of proximal ejecta from the orientale basin from lunar orbiter laser altimeter (LOLA) data: implications for multi-ring basin formation. Geophys. Res. Lett 38, L17201. doi:10.1029/2011GL048502.

Fassett, C.I., Head, J.W., Kadish, S.J., Mazarico, E., Neumann, G.A., Smith, D.E., Zuber, M.T., 2012. Lunar impact basins: stratigraphy, sequence and ages from superposed impact crater populations measured from lunar orbiter laser altimeter (LOLA) data. J. Geophys. Res. 117, E00H06. doi:10.1029/2011JE003951.

Garrick-Bethell, I., Zuber, M.T., 2009. Elliptical structure of the lunar South Pole–Aitken basin. Icarus 204, 399–408. doi:10.1016/j.icarus.2009.05.032.

Gault, D.E., Wedekind, J.A., 1978. Experimental studies of oblique impact. In: Proceedings of the Lunar and Planetary Science Conference, 9. „ HoustonTX, pp. 3843–3875.

Gruener, J.E., Joosten, B.K., 2009. NASA Constellation program office regions of interest on the Moon: a representative basis for scientific exploration, resource potential, and mission operations, 6036 (abstract). In: Mackwell, S.J. (Ed.), Lunar Reconnaissance Orbiter Science Targeting Meeting Report. Arizona State University, Tempe, AZ 58pp.

Haruyama, J., Ohtake, M., Matsunaga, T., Morota, T., Honda, C., Yokota, Y., Abe, M., Ogawa, Y., Miyamoto, H., Iwasaki, A., Pieters, C.M., Asada, N., Demura, H., Hirata, N., Terazono, J., Sakasi, S., Saiki, K., Yamaji, A., Torii, M., Josset, J-L., 2009. Long-lived volcanism on the lunar farside revealed by SELENE Terrain camera. Science 323, 905–908. doi:10.1126/science.1163382.

Hurwitz, D.M., Kring, D.A., 2014. Differentiation of the South Pole–Aitken basin impact melt sheet: implications for lunar exploration. J. Geophys. Res. Planets 119, 1110–1133. doi:10.1002/2013JE004530.

Ismail, I.A.H., Murrell, S.A.F., 1990. The effect of confining pressure on stress-drop in compressive rock fracture. Tectonophysics 175, 237–248. doi:10.1016/0040-1951(90)90140-4.

Ivanov, B.A., 2005. Numerical modeling of the largest terrestrial meteorite craters. Sol. Syst. Res. 39, 381–409. doi:10.1007/s11208-005-0051-0.

Ivanov, B.A., Melosh, H.J., Pierazzo, E., 2010. Basin-forming impacts: reconnaissance modeling. In: Reimold, W.U., Gibson, R.L. (Eds.). In: Large Meteorite Impacts and Planetary Evolution IV, 465. Geological Society of America, pp. 29–49. doi:10.1130/2010.2465(03), Special Paper.

Johnson, B.C., Blair, D.M., Collins, G.S., Melosh, H.J., Freed, A.M., Taylor, G.J., Head, J.W., Wieczorek, M.A., Andrews-Hanna, J.C., Nimmo, F., Keane, J.T., Miljković, K., Soderblom, J.M., Zuber, M.T., 2016. Formation of the Orientale lunar multiring basin. Science 354, 441–444. doi:10.1126/science.aag0518.

Jolliff, B.L., Gillis, J.J., Haskin, L.A., Korotev, R.L., Wieczorek, M.A., 2000. Major lunar crustal Terranes: surface expressions and crust-mantle origins. J. Geophys. Res. 105, 4197–4216. doi:10.1029/1999JE001103.

Jolliff, B.L., Shearer, C.K., Papanastassiou, D.A.MoonRise Science Team, 2017. Why do we need samples from the Moon's South Pole–Aitken basin and what would we do with them. Lunar Planet. Sci 48, 1300 abstract.

Klima, R.L., Pieters, C.M., Boardman, J.W., Green, R.O., Head, J.W., Isaacson, P.J., Mustard, J.F., Nettles, J.W., Petro, N.E., Staid, M.I., Sunshine, J.M., Taylor, L.A., Tompkins, S., 2011. New insights into lunar petrology: distribution and composition of prominent low-Ca pyroxene exposures as observed by the Moon mineralogy mapper (M^3). J. Geophys. Res. 116, E00G06. doi:10.1029/2010JE003719.

Kring, D.A., Kramer, G.Y., Collins, G.S., Potter, R.W.K., Chandnani, M., 2016. Peak-ring structure and kinematics from a multi-disciplinary study of the Schrödinger impact basin. Nat. Comm 7, 13161. doi:10.1038/ncomms13161.

McGetchin, T.R., Settle, M., Head, J.W., 1973. Radial thickness variation in impact crater ejecta, implication for lunar basin deposits. Earth Planet. Sci. Lett. 20, 226–236. doi:10.1016/0012-821X(73)90162-3.

Melosh, H.J., 1979. Acoustic fluidization: a new geologic process. J. Geophys. Res. 84, 7513–7520.

Melosh, H.J., Ivanov, B.A., 1999. Impact crater collapse. Annu. Rev. Earth Planet. Sci. 27, 385–415. doi:10.1146/annurev.earth.27.1.385.

Miljkovic, K., Wieczorek, M.A., Collins, G.S., Laneuville, M., Neumann, G.A., Melosh, H.J., Solomon, S.C., Phillips, R.J., Smith, D.E., Zuber, M.T., 2013. Asymmetric distribution of lunar impact basins caused by variations in target properties. Science 342, 724–726. doi:10.1126/science.1243224.

Miljković, K., Collins, G.S., Wieczorek, M.A., Johnson, B.C., Soderblom, J.M., Neumann, G.A., Zuber, M.T., 2016. Subsurface morphology and scaling of lunar impact basins. J. Geophys. Res. 121, 1695–1712. doi:10.1002/2016JE005038.

Morbidelli, A., Marchi, S., Bottke, W.F., Kring, D.A., 2012. A sawtooth-like timeline for the first billion years of lunar bombardment. Earth Planet. Sci. Lett. 355–356, 144–151. doi:10.1016/j.epsl.2012.07.037.

Moriarty, D.P., Pieters, C.M., 2016. South Pole–Aitken basin as a probe to the lunar interior. Lunar Planet. Sci. 47, 1763 abstract.

Morrison, D.A., 1998. Did a thick South Pole–Aitken basin melt sheet differentiate to form cumulates. Lunar. Planet. Sci. 29, 1657 abstract.

Neumann, G.A., Zuber, M.T., Wieczorek, M.A., Head, J.W., Baker, D.M.H., Solomon, S.C., Smith, D.E., Lemoine, F.G., Mazarico, E., Sabaka, T.J., Goossens, S.J., Melosh, H.J., Phillips, R.J., Asmar, S.W., Konopliv, A.S., Williams, J.G., Sori, M.M., Soderblom, J.M., Miljković, K., Andrews-Hanna, J.C., Nimmo, F., Kiefer, W.S., 2015. Lunar impact basins revealed by gravity recovery and interior laboratory measurements. Sci. Adv. 1. doi:10.1126/sciadv.1500852.

Ohtake, M., Uemoto, K., Yokota, Y., Morota, T., Yamamoto, S., Nakamura, R., Haruyama, J., Iwata, T., Matsunaga, T., Ishihara, Y., 2014. Geologic structure generated by large-impact basin formation observed at the South Pole–Aitken basin on the Moon. Geophys. Res. Lett. 41, 2738–2745. doi:10.1002/2014GL059478.

O'Sullivan, K.M., Kohout, T., Thaisen, K.G., Kring, D.A., 2011. Calibrating several key lunar stratigraphic units representing 4 b.y. of lunar history within Schrödinger basin. In: Williams, D.A., Ambrose, W. (Eds.). In: Recent Advances in Lunar Stratigraphy, 477. Geological Society of America, pp. 117–127. doi:10.1130/2011.2477(05), Special Paper.

Petro, N.E., Jolliff, B.L., 2013. Thin crust in the South Pole–Aitken basin and samples from the mantle? Implications for South Pole–Aitken basin sampling in light of recent GRAIL results. Lunar Planet. Sci. 44, 2724 abstract.

Petro, N.E., Sunshine, J., Pieters, C., Klima, R., Boardman, J., Besse, S., Head, J., Isaacson, P., Taylor, L., Tompkins, S., 2010. Lower crustal materials exposed in the Apollo basin revealed using Moon Mineralogy Mapper (M^3) data. Lunar Planet Sci. 41, 1802 (abstract).

Petro, N.E., Mest, S.C., Teich, Y., 2011. Geomorphic terrains and evidence for ancient volcanism within northeastern South Pole–Aitken basin. In: Ambrose, W.A., Williams, D.A. (Eds.). In: Recent Advances and Current Research Issues in Lunar Stratigraphy, 477. Geological Society of America, pp. 129–140. doi:10.1130/2011.2477(06), Special Paper.

Pierazzo, E., Melosh, H.J., 2000. Melt production in oblique impacts. Icarus 145, 252–261. doi:10.1006/icar.1999.6332.

Pieters, C.M., Head, J.W., Gaddis, L., Jolliff, B.L., Duke, M., 2001. Rock types of South Pole–Aitken basin and extent of basaltic volcanism. J. Geophys. Res. 106, 28001–28022. doi:10.1029/2000JE001414.

Pike, R.J., Spudis, P.D., 1987. Basin-ring spacing on the Moon, Mercury, and Mars. Earth Moon Planets 39, 129–194.

Potter, R.W.K., 2012. Numerical Modeling of Basin-Scale Impact Crater Formation Ph.D. Thesis. Imperial College London, London, England.

Potter, R.W.K., Collins, G.S., Kiefer, W.S., McGovern, P.J., Kring, D.A., 2012a. Constraining the size of the South Pole–Aitken basin impact. Icarus 220, 730–744. doi:10.1016/j.icarus.2012.05.032.

Potter, R.W.K., Kring, D.A., Collins, G.S., Kiefer, W.S., McGovern, P.J., 2012b. Estimating transient crater size using the crustal annular bulge: insights from numerical modeling of lunar basin-scale impacts. Geophys. Res. Lett. 39, L18203. doi:10.1029/2012GL052981.

Potter, R.W.K., Kring, D.A., Collins, G.S., Kiefer, W.S., McGovern, P.J., 2013. Numerical modeling of the formation and structure of the Orientale impact basin. J. Geophys. Res. Planets 118, 963–979. doi:10.1002/jgre.20080.

Potter, R.W.K., Kring, D.A., Collins, G.S., 2015. Scaling of basin-sized impacts and the influence of target temperature. In: Osinski, G.R., Kring, D.A. (Eds.). In: Large Meteorite Impacts and Planetary Evolution V, 518. Geological Society of America, pp. 99–113. doi:10.1130/2015.2518(06), Special Paper.

Potts, N.J., Gullikson, A.L., Curran, N.M., Dhaliwal, J.K., Leader, M.K., Rege, R.N., Klaus, K.K., Kring, D.A., 2015. Robotic traverse and sample return strategies for a lunar farside mission to the Schrödinger basin. Adv. Space Res. 55, 1241–1254. doi:10.1016/j.asr.2014.11.028.

Shearer, C.K., Elardo, S.M., Petro, N.E., Borg, L.E., McCubbin, F.M., 2015. Origin of the lunar highlands Mg-suite: an integrated petrology, geochemistry, chronology, and remote sensing perspective. Am. Mineral. 100, 294–325. doi:10.2138/am-2105-4817.

Shimada, M., Cho, A., Yukutake, H., 1983. Fracture strength of dry silicate rocks at high confining pressures and activity of acoustic emission. Tectonophysics 96, 159–172. doi:10.1016/0040-1951(83)90248-2.

Shoemaker, E.M., Robinson, M.S., Eliason, E.M., 1994. The south pole region of the moon as seen by clementine. Science 266, 1851–1854. doi:10.1126/science.266.5192.1851.

Stesky, R.M., Brace, W.F., Riley, D.K., Bobin, P.Y., 1974. Friction in faulted rock at high temperature and pressure. Tectonophysics 23, 177–203. doi:10.1016/0040-1951(74)90119-X.

Stuart-Alexander, D.E., 1978. Geologic map of the central far side of the Moon. United States Geological Survey map 1-1047, scale 1:5,000,000.

Vaughan, W.M., Head, J.W., 2014. Impact melt differentiation in the South Pole–Aitken basin: some observations and speculations, Planet. Space Sci 91, 101–106. doi:10.1016/j.pss.2013.11.010.

Wang, Q., Liu, J., 2016. A Chang'e-4 mission concept and vision of future Chinese lunar exploration activities. Acta Astronaut. 127, 678–683. doi:10.1016/j.actaastro.2016.06.024.

Whitten, J.L., Head, J.W., 2015. Lunar cryptomaria: physical characteristics, distribution, and implications for ancient volcanism. Icarus 247, 150–171. doi:10.1016/j.icarus.2014.09.031.

Wieczorek, M.A., Neumann, G.A., Nimmo, F., Kiefer, W.S., Taylor, G.J., Melosh, H.J., Phillips, R.J., Solomon, S.C., Andrews-Hanna, J.C., Asmar, S.W., Konopliv, A.S., Lemoine, F.G., Smith, D.E., Watkins, M.M., Williams, J.G., Zuber, M.T., 2013. The crust of the Moon as seen by GRAIL. Science 339, 671–675. doi:10.1126/science.1231530.

Wilhelms, D.E., 1987. The geological history of the Moon. In: U.S. Geological Survey Professional Paper 1348. United States Government Printing Office, Washington, D.C, p. 302.

Wünnemann, K., Collins, G.S., Melosh, H.J., 2006. A strain-based porosity model for use in hydrocode simulations of impacts and implications for transient crater growth in porous targets. Icarus 180, 514–527. doi:10.1016/j.icarus.2005.10.013.

Yamamoto, S., Nakamura, R., Matsunaga, T., Ogawa, Y., Ishihara, Y., Morota, T., Hirata, N., Ohtake, M., Hiroi, T., Yokota, Y., Haruyama, J., 2010. Possible mantle origin of olivine around lunar impact basins detected by SELENE. Nat. Geosci. 3, 533–536. doi:10.1038/ngeo897.

Yamamoto, S., Nakamura, R., Matsunaga, T., Ogawa, Y., Ishihara, Y., Morota, T., Hirata, N., Ohtake, M., Hiroi, T., Yokota, Y., Haruyama, J., 2012. Olivine-rich exposures in the South Pole–Aitken basin. Icarus 218, 331–344. doi:10.1016/j.icarus.2011.12.012.

Yingst, A., Head, J.W., 1999. Geology of mare deposits in South-Pole Aitken basin as seen by Clementine UVVIS data. J. Geophys. Res. 104 (E8), 18957–18979. doi:10.1029/1999JE900016.

Zhu, M.-H., Wünnemann, K., Potter, R.W.K., 2015. Numerical modeling of the ejecta distribution and formation of the orientale basin on the Moon. J. Geophys. Res. Planets 120, 2118–2134. doi:10.1002/ 2015JE004827.

Zuber, M.T., Smith, D.E., Neumann, G.A., Goossens, S., Andrews-Hanna, J.C., Head, J.W., Kiefer, W.S., Asmar, S.W., Konopliv, A.S., Lemoine, F.G., Matsuyama, I., Melosh, H.J., McGovern, P.J., Nimmo, F., Phillips, R.J., Solomon, S.C., Taylor, G.J., Watkins, M.M., Wieczorek, M.A., Williams, J.G., Jansen, J.C., Johnson, B.C., Keane, J.T., Mazarico, E., Miljković, K., Park, R.S., Soderblom, J.M., Yuan, D-N., 2016. Gravity field of the orientale basin from the gravity recovery and interior laboratory mission. Science 354, 438–441. doi:10.1126/science.aag0519.